Forward modeling of bending angles with a two-dimensional operator for GNSS airborne radio occultations in atmospheric rivers

P. Hordyniec[1,2], J. S. Haase[2], M. J. Murphy, Jr.[3,4], B. Cao[2], A. M. Wilson[5], I. H. Banos[6]

[1]Institute of Geodesy and Geoinformatics, Wrocław University of Environmental and Life Sciences, Wrocław, Poland
[2]Scripps Institution of Oceanography, University of California San Diego, La Jolla, California, USA
[3]Global Modeling and Assimilation Office, NASA Goddard Space Flight Center, Greenbelt, Maryland, USA
[4]GESTAR-II, University of Maryland Baltimore County, Baltimore, Maryland, USA
[5]Center for Western Weather and Water Extremes, Scripps Institution of Oceanography, University of California San Diego, La Jolla, California, USA
[6]NSF NCAR Mesoscale and Microscale Meteorology Laboratory, Boulder, Colorado, USA

Key Points:

- A two-dimensional forward model allows improved representation of bending angle profiles collected in critical areas of atmospheric rivers.
- Forward modeling with the tangent point drift mitigates bending angle departures of 5 % at the top of profiles.
- Significant contributions of horizontal gradients in the vicinity of atmospheric rivers can lead to departures of up to 20 %.

Corresponding author: Jennifer S. Haase, jhaase@ucsd.edu

Abstract

The Global Navigation Satellite System (GNSS) airborne radio occultation (ARO) technique is used to retrieve profiles of the atmosphere during reconnaissance missions for atmospheric rivers (ARs) on the west coast of the United States. The measurements are a horizontal integral of refractive index over long ray-paths extending between a spaceborne transmitter and a receiver onboard an aircraft. A specialized forward operator is required to allow assimilation of ARO observations into numerical weather prediction models to support forecasting of ARs. A two-dimensional (2D) bending angle operator is proposed to enable capturing key atmospheric features associated with strong ARs. Comparison to a one-dimensional (1D) forward model supports the evidence of large bending angle departures within 3-7 km impact heights for observations collected in a region characterized by the integrated water vapor transport (IVT) magnitude above 500 kg $m^{-1}s^{-1}$. The assessment of the 2D forward model for ARO retrievals is based on a sequence of six flights leading up to a significant AR precipitation event in January 2021. Since the observations often sampled regions outside the AR where moisture is low, the significance of horizontal variations is obscured in the average bending angle statistics. However, examples from an individual flight preferentially sampling the cross-section of an AR further support the need for the 2D forward model for targeted ARO observations. Additional simulation experiments are performed to quantify forward modeling errors due to tangent point drift and horizontal gradients suggesting contributions on the order of 5 % and 20 %, respectively.

Plain Language Summary

Atmospheric rivers (ARs) bring intense rainfall to the west coast of the United States. Reconnaissance missions make additional measurements from aircraft, such as dropsondes, in the near storm environment within the high moisture region of ARs. An airborne radio occultation (ARO) observation system was installed on the same aircraft to use Global Navigation Satellite System (GNSS) signals such as the Global Positioning System (GPS) to retrieve additional profile observations during flights. In order to use the ARO observations for weather forecasting, an observation operator is required to simulate observations based on the current atmospheric state and compare them to the actual measurements. In the region near the core of the AR where there are large horizontal contrasts in moisture, an accurate forward model must take into account the two-dimensional (2D) structure of atmosphere. This paper describes the development and testing of the 2D observation operator for ARO observations. The performance of the operator is verified based on a case study of a long sequence of six flights on consecutive days. The 2D forward model is shown to better represent observations collected in ARs, especially when sampling a well-formed mid-latitude AR with a large contrast in properties across the cold front.

1 Introduction

Atmospheric rivers (ARs) play a vital role in the global water cycle by transporting tropical moisture poleward (Guan et al., 2021). In particular, landfalling ARs are the key drivers of floods and provide the majority of the water supply in western North America, where they frequently produce significant amounts of rainfall or snow over mountainous regions (Gershunov et al., 2017; Dettinger et al., 2011; Ralph et al., 2006). An AR is defined as a long, narrow filament of high integrated vapor transport (IVT) often identified by an IVT minimum threshold of 250 kg m^{-1} s^{-1} (Ralph et al., 2019). Accurate predictions of AR landfall location and intensity are required to support flood mitigation and water resource management. To support accurate weather predictions, global operational numerical weather prediction (NWP) models assimilate observations to improve their representation of the initial state of the atmosphere. There are limited conventional meteorological observations over the remote areas of the northeast Pacific Ocean where ARs typically develop, and hence, there is a high reliance on remotely sensed observations from satellites. These satellites may fail to capture key atmospheric features of a particular event due to their spatial and temporal sampling characteristics, or have difficulty observing through the clouds and hydrometeors that are often associated with ARs (Zheng, Delle Monache, Wu, et al., 2021). Near-surface and all-weather observations of high vertical resolution are required to supplement satellite radiance in regions of dense clouds (Ralph et al., 2017) to accurately observe AR characteristics and structure since most of the water vapor transport within an AR occurs in the lowest 3 km.

The Atmospheric River Reconnaissance (AR Recon) program is a collaborative international, interagency effort led by the Center for Western Weather and Water Extremes (CW3E) that was developed in part to address this observation gap. AR Recon is aimed at improving predictions of ARs and their impacts at lead times of 1-5 days by collecting targeted observations disseminated in real-time for operational assimilation into NWP models (Zheng, Delle Monache, Cornuelle, et al., 2021). The foundational AR Recon observations are dropsonde profiles (Ralph et al., 2020; Office, 2022). Complementary remote sensing observations using the GNSS airborne radio occultation (ARO) technique in a limb-viewing geometry allow simultaneous retrieval of atmospheric profiles that sample the near storm environment surrounding the dropsondes at no additional expendable cost (Haase et al., 2014). The closely matched geolocations of in-situ soundings from dropsondes also provide an independent nearby reference for improved understanding of the information collected in AR events with ARO. A number of sensitivity studies have been carried out to assess ARO measurement uncertainties and optimize retrieval methodologies for sampling AR environments or other challenging atmospheric phenomena (Xie et al., 2008; Muradyan et al., 2011; Xie et al., 2018). Further improvements in the receiver software algorithms through the implementation of the open-loop (OL) tracking (Wang et al., 2016) and development of radio-holographic inversion methods (Adhikari et al., 2016; Wang et al., 2017) allowed sensing the lowermost troposphere with ARO while reducing the inversion errors due to multipath propagation. This additional OL tracking capability is currently being added to ARO operations as part of AR Recon. Ultimately, ARO measurements can benefit AR science through their assimilation into NWP models, thus contributing to improvements in model initial conditions and forecast skill (Haase et al., 2021; X. M. Chen et al., 2018).

In order to achieve this goal, a computationally efficient and accurate forward operator is needed to allow realistic modeling of observations in strongly varying AR environments. Following developments in assimilation methods for spaceborne RO (Healy & Thépaut, 2006; Cucurull et al., 2007, 2013; Healy et al., 2007), the geophysical variable of bending angle is preferred over refractivity since bending angle is a more "raw" observable affected by fewer assumptions about the state of the atmosphere and generally has simpler error characteristics (Eyre et al., 2022). However, bending angle operators are inherently more complex and computationally demanding than those for refractivity. This is due to bending angle being derived from numerical integration of a profile of refractive index from a given background atmospheric state using the Abel integral (Fjeldbo et al., 1971; Melbourne et al., 1994; Kursinski et al., 1997). Among the assumptions implicit in the Abel integral is a horizontally symmetric atmosphere, leading to any observation operator employing it to be one-dimensional (1D). In contrast, the refractivity operator is essentially an interpolation of standard meteorological variables from an atmospheric model grid to locations of the ARO retrieval which is an intermediate step in the forward modeling of bending angles. More sophisticated, two-dimensional (2D) bending angle operators can account for horizontal gradients (Healy, 2001; Poli, 2004) in the atmosphere along the propagation path by solving the ray equations with numerical ray-tracing methods. In addition, the ARO profiles are not vertical, so to avoid that approximation, the operator can also take into account the drift of the tangent point location representing the ray-path position of the closest approach to the Earth's surface. Since the same principle applies to both spaceborne and airborne RO measurement concepts, the existing state-of-the-art bending angle operators (Healy et al., 2007; Ruston & Healy, 2021) used in the assimilation of neutral atmosphere profiles from leading satellite missions could be as well adapted for airborne RO retrievals after accounting for key differences in the measurement geometry. These are used operationally for the Formosa Satellite Mission 7 (FORMOSAT-7)/Constellation Observing System for Meteorology, Ionosphere and Climate 2 (hereafter COSMIC-2; (Anthes & Schreiner, 2019; Schreiner et al., 2020)), the European Organisation for the Exploitation of Meteorological Satellites (EUMETSAT)'s Meteorological Operational satellites program (MetOp; (von Engeln et al., 2009)), and commercial constellations.

The following study demonstrates the first implementation of forward modeling of ARO bending angles based on a modified 2D operator originally designed for spaceborne RO retrievals. This approach is motivated by the incorporation of the spaceborne 2D operator in the Joint Effort for Data assimilation Integration framework (JEDI;(Trémolet & Auligné, 2020)), led by the Joint Center for Satellite Data Assimilation (JCSDA), that implements observation operators as independent modules that are model-agnostic. Implementing the complementary version of the ARO 2D operator in JEDI makes it accessible to all operational NWP centers that are migrating to the new JEDI platform. Secondly, simulations with the newly developed forward model will aid in quantifying contributions of horizontal refractivity gradients to ARO bending angle retrievals. Third, the operator will allow an overall quality assessment of bending angle retrievals from ARO contributing to potential adjustments of existing observation error models required by data assimilation systems. Fourth, the assessed error characteristics will provide feedback and insight on how to improve ARO retrieval methodologies to further reduce the measurement uncertainties of targeted observations collected within ARs to benefit future AR Recon or tropical cyclone field campaigns.

In this work, we first describe the observational datasets collected during the 2021 AR Recon campaign followed by a synoptic overview of a specific high impact AR event in section 3. In section 4 we outline key characteristics of the 2D bending angle observation operator for ARO. Section 5 presents observation minus simulated (also commonly referred to as innovations or residuals) bending angle statistics to support the estimation of the observation error model. Forward modeling errors due to the effect of tangent point drift and horizontal refractivity gradients are discussed in section 6. A case study analysis is provided in section 7 and the conclusions are given in section 8.

2 Observational Datasets

Specially targeted weather reconnaissance flights took place over the northeast Pacific Ocean as a part of AR Recon 2021 in support of operational NWP forecasts of AR events in the western United States (Ralph et al., 2020). Of the 29 intensive observation periods (IOPs) during AR Recon 2021, six are selected for the present study from IOP03 through IOP08. These IOPs are part of a sequence that sampled an impactful AR on consecutive days from early in its development on 23 January 2021 through landfall in central California on 28 January 2021 (Figure 1). These sequential flights were planned based on research showing that the impact of dropsonde observations on forecasts is higher when the event is sampled on multiple consecutive days (Zheng, Delle Monache, Cornuelle, et al., 2021).

Each of these six IOPs is centered at 0000 Coordinated Universal Time (UTC) and includes observations from the National Oceanic and Atmospheric Administration (NOAA) Gulfstream IV (G-IV) aircraft, which has an average cruising altitude of 14 km. In addition to the NOAA G-IV, two United States Air Force Reserve Command 53rd Weather Reconnaissance Squadron WC-130J aircraft, which have an average cruising altitude of 9 km, are deployed during IOP04 and a single WC-130J is employed during IOP07 and

IOP08. Observations collected from all of these aircraft include dropsondes profiles of pressure, temperature, humidity, and wind. The NOAA G-IV is equipped with a GNSS receiver to retrieve geophysical profiles from ARO measurements for all of these IOPs. The ARO receiver deployed onboard the NOAA G-IV aircraft during AR Recon 2021 has the capability of tracking dual-frequency signals from GPS, GLONASS, and Galileo constellations, providing more occultations and thus resulting in improved spatial and temporal sampling relative to conventional GPS-only observations. The G-IV flight level in-situ observations of pressure, temperature, and humidity are used in the retrieval of the ARO profiles.

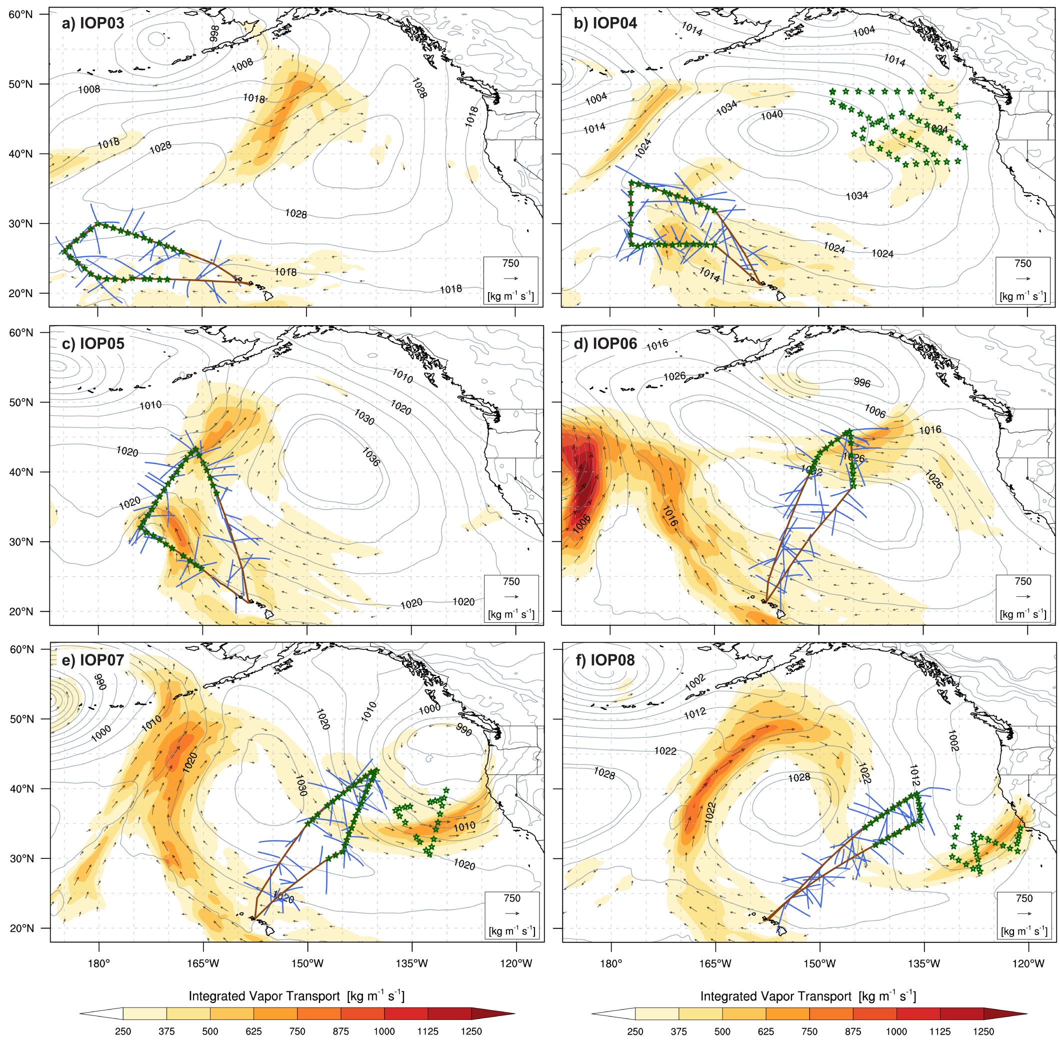

Figure 1. Overview of the six consecutive intensive operating periods (IOPs) selected from the AR Recon 2021 campaign that were centered at 00 UTC on 23 through 28 January 2021. Integrated vapor transport (kg m^{-1} s^{-1}, shaded and vectors) and mean sea level pressure (hPa, grey contours) are shown with the locations of dropsondes (green stars), airborne radio occultation tangent point profiles (blue lines), and the flight path of the NOAA G-IV aircraft (brown lines) overlain. The flight path(s) of WC-130J aircraft are not shown though dropsondes from these flights are indicated.

2.1 Airborne radio occultations

ARO retrievals result in significantly slanted profiles due to the aircraft flying at much slower speeds relative to GNSS satellites resulting in a horizontal spread of observations within a single ARO event. The point of the closest approach to the Earth's surface for an individual ray-path is referred to as the tangent point. The tangent point is near the aircraft at the top of the profile and the furthest from the aircraft at the lowest point. Figure 1 shows a total of 280 ARO profiles that are retrieved from six IOPs, with occultation counts per flight varying from 36 for IOP03 to 51 for IOP06. An ARO profile is referenced to a single representative location indicated by the reference tangent point that corresponds to the lowermost observed profile point in the ARO retrieval. In addition, an ARO profile contains individual geolocations at each height to enable assimilation that accounts for tangent point drift.

The ARO equipment deployed includes a GNSS signal recorder for making very low altitude observations, however the results presented here are from the ARO receiver which tracks signals with a phase-locked loop. Phase fluctuations from complex atmospheric multipath propagation typically terminate phase-locked loop signal tracking before sampling the lowest part of the troposphere, such that retrieved profiles reach an average of 4 km above the surface (Fig. 2). Fewer than 20 occultations penetrate to the lowermost troposphere below 2 km. In the retrieval procedure, the aircraft position is first estimated with an accuracy better than 30 cm using Precise Point Positioning with ambiguity resolution (Geng et al., 2019), then the excess path length of the radio signal is calculated relative to a straight-line distance between the aircraft and a GNSS satellite. The first-order ionospheric delay in the neutral atmosphere retrievals is mitigated by the linear combination of dual-frequency observations and applied to the excess phase at each sample time (B. Murphy et al., 2015). Prior to inversion to the bending angle, the excess phase is smoothed with a second-order Savitzky-Golay filter in an 11 s window to eliminate fluctuations with scales shorter than the first Fresnel zone (Cao et al., 2022). Then the ionosphere-corrected smoothed excess phase is inverted to bending angle in the geometrical optics approach assuming single-ray propagation (Xie et al., 2008).

The bending accumulated inside the atmosphere below the aircraft height along two symmetrical sections of the ray path around the tangent point corresponds to the ARO observable of 'partial' bending angle. The refraction along the ray-path section continuing outwards to the higher atmosphere in the direction of a GNSS transmitter contributes to the additional bending, which together with the 'partial' bending yields the 'full' bending angle of the ray-path. In general, the magnitude of the 'partial' bending is slightly smaller than that of the corresponding 'full' bending angle due to relatively small refractivity contributions above the aircraft height. However, the bending above the receiver cannot be measured directly from observed Doppler shifts. Instead, this additional contribution needs to be separated with the use of auxiliary atmospheric information to derive the 'partial' bending angle. This can be either from an ARO ray-path arriving at the antenna at the same angle above the horizon as the observation is below the horizon, assuming spherical symmetry (Healy et al., 2002), or from ray-tracing of an assumed profile above the aircraft height (B. Murphy et al., 2015). Retrieved bending angles can be further inverted to profiles of refractive index with the modified Abel transform (Healy et al., 2002; Xie et al., 2008) under the assumption of local spherical symmetry. Since the aircraft is flying within the atmosphere, the Abel inversion is constrained at the top of the profile by in-situ refractivity calculated from flight-level pressure, temperature, and moisture measurements retrieved from meteorological sensors onboard the aircraft (Cao et al., 2024). When in-situ moisture measurements are unreliable at high altitudes, the moisture contribution to in-situ refractivity is neglected. According to sensitivity studies (Xie et al., 2008), the in-situ measurement error mostly affects ARO retrievals within 1 km of the aircraft flight level. No statistical optimization is applied to

ARO retrievals as the ionospheric residual noise is generally not expected to exceed the atmospheric contribution to the bending at or below the aircraft height.

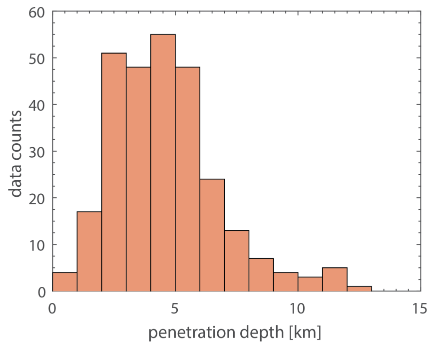

Figure 2. Histogram showing the lowest geometric altitude sampled by the ARO profiles from six IOPs during AR Recon 2021.

2.2 Reanalyses

The reanalysis product chosen to represent the state of the atmosphere during AR Recon 2021 is the European Centre for Medium-Range Weather Forecasts (ECMWF) Renalysis 5 (ERA5; Hersbach et al. (2020)). The ERA5 reanalysis has been shown to provide a useful representation of precipitation for North America with quality comparable to observations (Tarek et al., 2020). The atmospheric state depicted in the ERA5 is used for simulating the ARO bending angle for the comparisons shown herein. These are obtained from the ECMWF data catalogue already interpolated to a regular latitude-longitude grid with 0.25°×0.25° resolution in the horizontal, on the native 137 hybrid sigma levels in the vertical, and at 1-hourly temporal resolution. Meteorological variables used from ERA5 are the temperature, specific humidity, geopotential, integrated water vapor (IWV) and the magnitude of IVT which was derived from the components of the IVT vector in the zonal and meridional directions. The atmospheric pressure at each level is calculated with the use of surface pressure provided in the form of natural logarithm and model-defining coefficients at the interfaces (half-levels) between the native levels of the model.

3 Synoptic overview of the atmospheric river event

The aforementioned AR event chosen as the case study for evaluation of the ARO operator made landfall in California on 27 January 2021 and brought widespread impacts throughout the state. Parts of central California were under AR conditions for almost 48 hours with AR2 conditions on the AR scale (Ralph et al., 2019). The AR was associated with over 175 mm of precipitation in parts of the Sierra Nevada, Central Coast, and Transverse mountain ranges. This led to flooding with damaging debris flows and road closures in central and southern California.

The sampling of this event by a reconnaissance aircraft began on 23 January 2021 (IOP03, Fig. 1), in which the target of the NOAA G-IV was the region of development of an extratropical cyclone (ETC) as indicated by model forecasts and sensitivity metrics (not shown) monitored during AR Recon (Reynolds et al., 2019). The targeted ETC began forming at lower latitudes near the Hawaiian Islands as a Kona Low (Daingerfield, 1921; Simpson, 1952; Ramage, 1962). While the development and track of Kona Lows have proven difficult for NWP models to predict, they can be a key element driving the evolution of ARs (Morrison & Businger, 2001; S. Chen et al., 2022) and hence an excellent target for AR Recon. By 25 January (IOP05) a closed mean sea level pressure (MSLP) contour can be seen at 31°N, 173°W indicating the presence of the Kona Low at the surface on the southwestern flank of a large anticyclone centered at 42°N, 146°W. This area was among the target regions sampled by the G-IV on this day as part of IOP05. The next day, a different ETC was intensifying in the Gulf of Alaska to the northeast of the anticyclone and the IVT in a developing AR in the region of enhanced MSLP gradient between the ETC in the Gulf of Alaska and the anticyclone was sampled by the G-IV aircraft as part of IOP06. By 0000 UTC on 27 January the AR was making landfall in California and was sampled by a WC-130J aircraft (Fig. 1 green stars without a brown flight track underneath) while the main target of the G-IV was the trough to the west of the AR, a feature often associated with regions of high sensitivity to PV and potential temperature errors in forecasts for AR precipitation (Reynolds et al., 2019). On 28 January, again the target of the G-IV aircraft was a region of model sensitivity in the trough, and a WC-130J aircraft sampled the AR as it continued to make landfall as part of IOP08. In general during this sequence of IOPs, the focus of the G-IV is on the ETC and upper level dynamical features that could modulate AR structure and evolution, in addition to sampling the AR itself, while the WC-130J aircraft is focused on transects of the AR.

4 Two-dimensional bending angle forward model

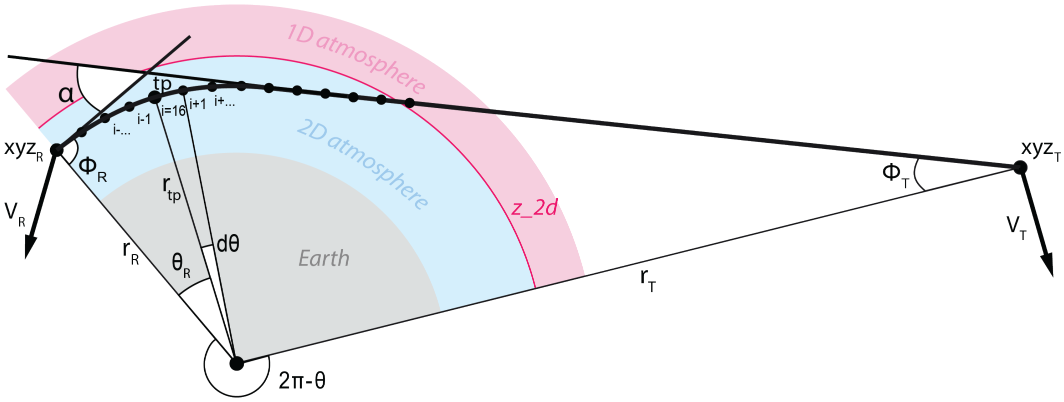

Figure 3. Schematic illustration of the geometry for airborne radio occultations. The central angle θ can be derived given known positions of the receiver xyz_R and the transmitter xyz_T at radii r_R, r_T, respectively. The angular separation $d\theta$ determines the points at which to extract model profiles between ray-path points i, $i+1$ along the occultation plane centered at $i = 16$ corresponding to the location of the observed tangent point (tp) having a radius r_{tp}. The central angle θ_R between the tangent point location and the receiver will not exactly match the angular separation $15 \times d\theta \approx 600$ km since model profiles are extracted beyond the receiver location (ray-path points not shown). The bending angle α is the difference between the incoming and outgoing ray-path direction. z_2d indicates the altitude limit for the 2D simulations and the atmosphere is assumed to be spherically symmetrical above.

Before we describe the key characteristics of the ARO forward model, the general features are recalled first to outline the configuration used in simulations of bending angles. The adopted forward model is based on the bending angle operator developed by ECMWF for spaceborne RO (Healy et al., 2007; Eyre, 1994). The operator, together with other forward modules, is available as a part of the Radio Occultation Processing Package (ROPP) (Culverwell et al., 2015) provided by the Radio Occultation Meteorology

Satellite Application Facility (ROM SAF). The technical description of the forward module can be found in the corresponding user guide (ROM SAF, 2021). The two-dimensional operator requires as input planar meteorological information extracted from gridded NWP fields along the occultation plane for an individual ray-path schematically shown in Fig. 3. The location of the tangent point and orientation of the occultation plane is provided in the ARO data structure in terms of latitude, longitude, height and azimuth with respect to the north towards a GNSS transmitter. The information is provided for individual impact parameters as well as for the reference location of the profile, which is at the tangent point representative of the lowest section of the retrieved profile. The planar information is composed of 31 vertical profiles extracted at equally-spaced locations using an angular separation $d\theta = 4.708837$ mrad, corresponding to the arc length of $\sim$40 km on a reference sphere having a radius $r = 6371$ km. The total horizontal span is $30 \times d\theta \approx 1200$ km. The ERA5 refractivity (N) on model levels is computed from a series of vertical profiles of standard meteorological variables based on provided air pressure (P_a), water vapor pressure (P_v) and temperature (T) following the two-term empirical formula (Smith & Weintraub, 1953)

$$N = 77.6\frac{P_a}{T} + 3.73 \times 10^5 \frac{P_v}{T^2} \tag{1}$$

without considering the effects of non-ideal gas compressibilities (Aparicio et al., 2009) that are available as a part of an optional routine. Then, the refractive-index radius product $\chi = nr = (1 + 10^{-6}N)r$ is pre-computed on model levels serving as a 2D input field to a ray-tracer for the calculation of bending angles. The integration is initialized at the central profile matching the location of the tangent point at the observed impact parameter p.

Two key aspects are outlined here to emphasize the differences between the simulated ray tracing in the airborne and spaceborne forward models. First, the signal arriving at the airborne receiver does not leave the atmosphere as in the spaceborne case. Hence, the distance inside the atmosphere along the ray-path from the tangent point to the receiver is not the same as the distance from the tangent point to the transmitter, even in a spherically symmetrical atmosphere. It is also advantageous to avoid the assumptions used to derive 'partial' bending angle from the 'full' bending angle in the context of data assimilation due to error correlations. Therefore, the 'full' bending angle is proposed as a preferred observable for simulations with the ARO forward model although only slight modifications to the ray-tracing algorithm are required to allow 'partial' bending angle modeling. Second, the bending angle profile is retrieved up to the aircraft altitude rather than continuing above up to the altitude of low Earth orbiting (LEO) satellite, as in spaceborne RO, where it is assumed to be a vacuum. Thus, the radius to the aircraft height must be known inside the ARO observation operator. The receiver height is not routinely provided as a part of RO atmospheric products distributed to operational centers, such as the Binary Universal Form for the Representation of meteorological data (BUFR) maintained by the World Meteorological Organization (WMO). In ARO retrievals, the top most point of the refractivity profile corresponds to the ray-path whose tangent point is at the aircraft height and location. The refractivity with its independent variable of mean sea level height (whose datum is the geoid) are both contained in the standard RO observation structure (Cao et al., 2024). Thus, storing the aircraft height variable separately and modifications to the data formats are not required. Together with the local radius of the curvature r_C and the geoid undulation u computed from the Earth Gravitational Model 1996 (EGM96), the receiver radius can be calculated as

$$r_R = r_C + u + h_{top} \ , \tag{2}$$

where h_{top} is mean sea level height of the tangent point at the top of the profile.

The ARO refractivity retrieval based on the Abel transform assumes the aircraft flight altitude is constant over the duration of the occultation, and this height is used as the upper limit of integration of bending angle over impact parameter for all the ray-paths (B. Murphy et al., 2015; Haase et al., 2014). This is not strictly true, however the NOAA G-IV aircraft cruise altitude is generally maintained throughout the flight for long segments with infrequent, short ascents of 200-300 m. B. J. Murphy (2015) showed that when the standard deviation of the aircraft height averaged over the duration of the occultation was less than about 150 m, the effect of the height variation was less than the limiting aircraft velocity error. Occultation profiles with large aircraft height variations are eliminated in the quality control and evaluation of the ARO dataset.

The asymmetry in the geometry of the ray-path in the atmosphere that is specific to ARO will affect the approach to the numerical solution of the ray-path equations when propagating the ray through the atmospheric model (Rodgers, 2000):

$$\begin{aligned} \frac{dr}{ds} &= cos\phi \ , \\ \frac{d\theta}{ds} &= \frac{sin\phi}{r} \ , \\ \frac{d\phi}{ds} &= - \ sin\phi \left[\frac{1}{r} + \frac{1}{n}\left(\frac{\partial n}{\partial r}\right)_{\theta}\right] + \frac{cos\phi}{nr}\left(\frac{\partial n}{\partial \theta}\right)_{r} \ , \end{aligned} \tag{3}$$

where n describes the refractive index of the atmosphere at a point on the ray-path, r and θ are polar coordinates of the point with origin at the center of curvature, s is the distance from the point to the next along the ray-path, ϕ is the angle between the local radius vector and the tangent to the ray-path at the point. The ray equation is integrated numerically starting from the observation tangent point location to the two end-points: (1) one on the side of the aircraft and (2) one on the side of the GNSS satellite as depicted in Fig. 3. The differential equations are solved with the fourth-order Runge-Kutta method. Once the radius of the aircraft is reached by the ray-path propagating in the direction of the receiver, the integration is terminated and the other side is evaluated. If the ray equation was terminated at the same radius on the side propagating toward the transmitter, the simulated geophysical variable would correspond to the 'partial' bending angle for ARO which is used in the refractivity retrieval. For the 'full' bending angle simulations, the ray-path continues propagating beyond the radius of the aircraft up to the height controlled by the parameter z_2d. For the simulations in this study z_2d is set to 20 km to be always above the typical aircraft cruising altitude of the NOAA G-IV at ∼14 km. The bending of the ray-path above the height z_2d is computed under the assumption of spherical symmetry using the Abel integral

$$\Delta\alpha_{1d}\left(p\right) = -p \int_{r_c + z\_2d}^{\infty} \frac{dln(n(\chi))}{d\chi} \frac{d\chi}{\sqrt{\chi^2 - p^2}}, \tag{4}$$

that is given in terms of Gaussian error function, with the refractive index n sourced from the nearest model profile at the central angle θ. The bending above the model top that for ERA5 with 137 levels typically reaches ∼75 km is accounted for by extrapolating

$$\Delta\alpha_{top} = 10^{-6}\sqrt{2\pi p k_j} N_j exp\left(k_j(\chi_j - p)\right)\left[1 - erf\left(k_j\left(\chi_j - p\right)\right)\right], \tag{5}$$

where the inverse of refractivity scale-height between subsequent model levels j, $j+1$ being at the model top is expressed with $k_j = ln(N_j/N_{j+1})/(\chi_{j+1}/\chi_j)$. The sum of bending of three segments of the ray-path (1) from the tangent point to the receiver, (2) from the tangent point to z_2d and (3) from z_2d to the model top with the extrapolation above yields the 'full' bending angle.

5 Characteristics of observation errors in ARO retrievals

Profiles of bending angle collected during the six IOPs are simulated with the observation operator using the ERA5 reanalysis for the assessment of uncertainties. The

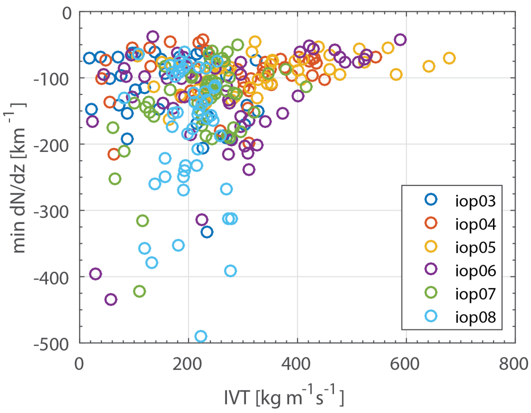

Figure 4. Relationship between IVT magnitudes and minimum vertical refractivity gradients (dN/dz) based on ERA5 profiles collocated with ARO retrievals at the location of reference tangent point.

statistics are computed as observed minus simulated bending angle for differences in absolute units, which are further divided by simulated value for fractional differences. Typically, the quality of RO observations is assessed based on globally distributed profiles that might capture variable atmospheric conditions from challenging vertical structures in the tropics to significantly drier environments in higher latitudes and polar regions. The two simplifying assumptions that are often made are that (1) the atmosphere is spherically symmetric and (2) there is no tangent point drift. Contributions of those assumptions to overall bending angle statistics when using an atmospheric model or reanalysis product as a reference have not yet been studied for ARO retrievals. Therefore, both (1) horizontal refractivity gradients and (2) tangent point drift are accounted for when simulating ARO observations at each observed tangent point location with the modified 2D forward model. This is particularly important for ARO targeted observations from AR Recon which are collected within AR environments associated with the high humidity pre-frontal low-level jet where strong gradients in moisture, and thus refractivity, are observed (Haase et al., 2021). Challenging atmospheric conditions for GNSS RO signal propagation are encountered in the presence of strong vertical gradients in the refractivity, where dN/dz $<$ -157 km^{-1} (Sokolovskiy, 2003). The advantage of using a 2D observation operator for spaceborne RO in ARs was quantified for bending angle innovations calculated from background forecasts from the operational Global Forecast System (GFS) model (M. J. Murphy et al., 2024) with the impact of the 2D operator increasing with increasing IVT.

The minimum in the refractivity gradient is a useful diagnostic for the detection of planetary boundary layer height (Xie et al., 2012; Basha & Ratnam, 2009) because the magnitude of dN/dz can be used to describe its sharpness (Guo et al., 2011). The condition dN/dz $<$ -157 km^{-1} suggests anomalous radio propagation associated with super-refraction which might result in large RO retrieval errors in the lowermost troposphere (Beyerle et al., 2003; Ao, 2007). We use the magnitude of dN/dz as an indicator of potential large bending angle deviations. Figure 4 shows the correspondence of IVT magnitudes to minimum refractivity gradients based on ERA5 profiles extracted at the location of reference tangent points for ARO observations during the six IOPs. The assessment shows that IVT magnitudes are weakly inversely correlated with refractivity gradients developing in the lower troposphere. The minima in dN/dz are often found below 4 km altitude with the strongest gradients developing at $\sim$1.5 km. The majority of strong dN/dz values occur in atmospheric conditions outside of ARs determined by the

IVT < 250 kg m^{-1} s^{-1} criterion. Most of the points with the strongest gradients of less than -200 km^{-1} are during IOP08 where IVT magnitudes are on the order of 200 kg m^{-1} s^{-1} and the aircraft sampled the dry and cold post-frontal region in the trough behind the targeted AR, where a sharp boundary layer typically develops. All the flights with strong negative gradients, IOP06, IOP07, and IOP08, flew a significant ferry over a subtropical pressure high northeast of Hawaii, where subsidence would also lead to a sharp boundary layer. In contrast, the intense AR sampled during IOP05 with IVT > 400 kg m^{-1} s^{-1} is characterized by refractive conditions with dN/dz ≈ -100 km^{-1}. The assessment of the dN/dz distribution is consistent with previously reported evidence of strong gradients developing in the lower troposphere outside of ARs based on dropsondes and spaceborne RO retrievals (Murphy Jr & Haase, 2022; Haase et al., 2021).

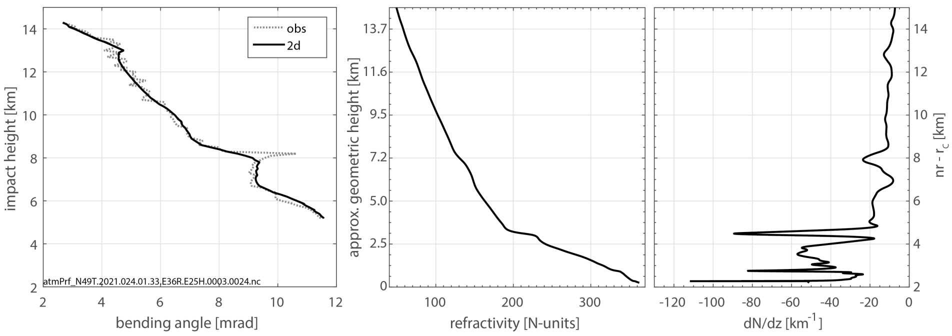

Figure 5. (left) Observed and 2D simulated bending angle profiles for one ARO occultation during IOP04. (middle) Refractivity calculated from ERA5 at the location of the central profile and (right) corresponding vertical refractivity gradient.

An example of an ARO bending angle profile from IOP04 in Fig. 5 is characterized by a prominent feature at ∼8 km impact height producing a bending angle spike that is typically observed in the presence of an inversion layer. The bending angle variation is reflected fairly well in the corresponding simulations. The refractivity field from the ERA5 at the height of the bending angle spike has a homogeneous horizontal distribution as indicated by the similarities between simulation results in 2D and 1D (not shown as it cannot be visually distinguished). The existence of an inversion layer is supported by several of the nearby dropsonde profiles at 168°N, 33°W on the east side of the low level moisture plume (see supplementary material and refer to `https://cw3e.ucsd.edu/arrecon_data/` for more dropsonde profiles and upper air charts). The inversion at ∼8 km is likely associated with the temperature difference between the air mass containing the upper level southwesterly jet with and the air mass beneath it with southerly winds. The inversion seen at 3 km in both the dropsonde and ERA5 appears to be the explanation for the termination of the ARO profile.

The penetration depth of the observed bending angle profile in Fig. 5 is affected by gradients developing in the lower troposphere with multiple inversion layers at and below 4 km, also observed in the nearby dropsonde profiles. The moderate magnitude of dN/dz > -120 km^{-1} from the ERA5 does not indicate super-refraction would occur, however, the dropsonde profiles illustrate the actual gradients could have larger magnitude. The dropsonde IVT of 340 kg m^{-1} s^{-1} indicates that the profile captures the tropical moisture export associated with the Kona low that eventually contributes to an AR.

The bending angle deviations between observations and 2D simulations for the six IOPs during AR Recon 2021 are presented in Fig. 6. We limit our assessment of observation errors to a more statistically representative range above 4 km impact height due to less than 10 % of the ARO profiles penetrating down to 2.5 km impact height (∼1 km

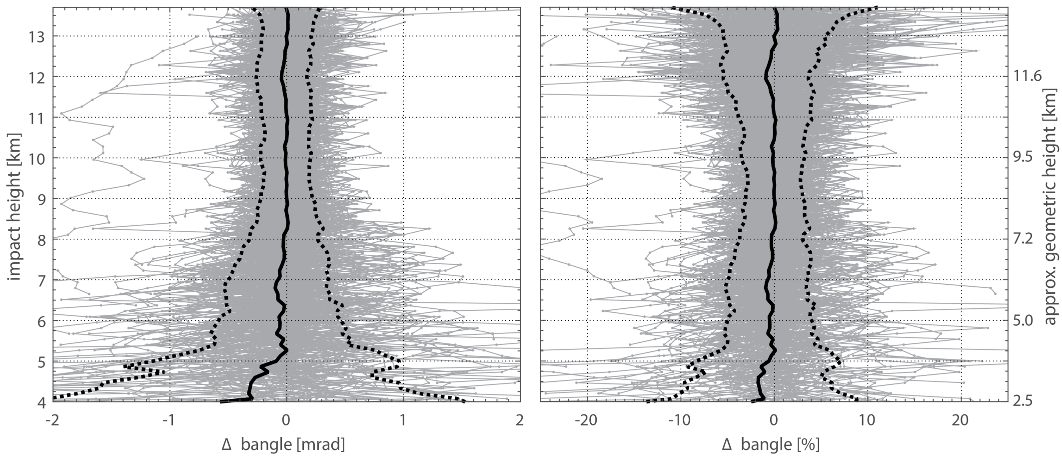

Figure 6. Observed minus 2D simulated bending angle deviations in (left) absolute and (right) fractional units for six IOPs during AR Recon 2021. Grey lines correspond to bending angle differences for individual profiles, the solid black line is the mean difference and dotted black lines show standard deviation.

geometric altitude in Fig. 2). The GNSS receiver measurements terminate due to challenging signal tracking conditions in the presence of strong refractivity gradients. Their existence further motivates future efforts towards analysis of data collected from the ARO advanced GNSS recorder and implementation of advanced radio-holographic ARO retrieval methods (Wang et al., 2016, 2017) to enable detection of inversion layers in the lowermost troposphere associated with ARs. The standard deviation at 4 km impact height is on the order of 10 % corresponding to absolute bending angle differences of 2 mrad. The standard deviation generally decreases with height up to ∼10 km. There is a slight increase in the standard deviation at 5 km due to outlying observations being affected by errors close to the lowest observed height where many of the ARO profiles terminate (Fig. 2). The mean difference also increases towards the surface, showing negative bias below 5 km impact height of -1.5 % which is equivalent to -0.3 mrad. The standard deviation in the middle troposphere is generally below 4 %. The increased error above 10 km impact height, visible in the fractional deviations, is expected due to the decrease in the magnitude of the bending angle relative to the limiting errors in knowledge of the aircraft velocity. Velocity errors map into excess Doppler (Muradyan et al., 2011) and can partially explain the oscillatory characteristics of the observed bending angles (Fig. 5). This potentially contributes to the slight negative bias not exceeding -1 % (-0.1 mrad) in bending angles at 12 km impact height. However, the noise level does affect the capability of ARO to resolve smaller amplitude atmospheric features above 10 km (Fig. 5). The optimal use of noise filtering methods (Cao et al., 2022) is required to further improve bending angle observations in the upper levels while preserving the vertical sensitivity of ARO. Despite this, ARO observations are effective at retrieving precise vertical information about variations in tropopause height in ARs (Haase et al., 2021) and in the equatorial atmosphere from balloon-borne RO (Cao et al., 2022), because of the large magnitude of the tropopause temperature variations.

In order to study the potential contribution of horizontal refractivity inhomogeneities to bending angle deviations, simulations utilizing 2D atmospheric fields from ERA5 are compared with results based on a 1D atmosphere. The spherically symmetrical refractivity field was provided as an input to the 2D forward model to simulate corresponding 1D bending angle profiles. For this case, the ERA5 refractivity at the central profile of the 2D field is repeated for 31 locations along the occultation plane. Figure 7 shows

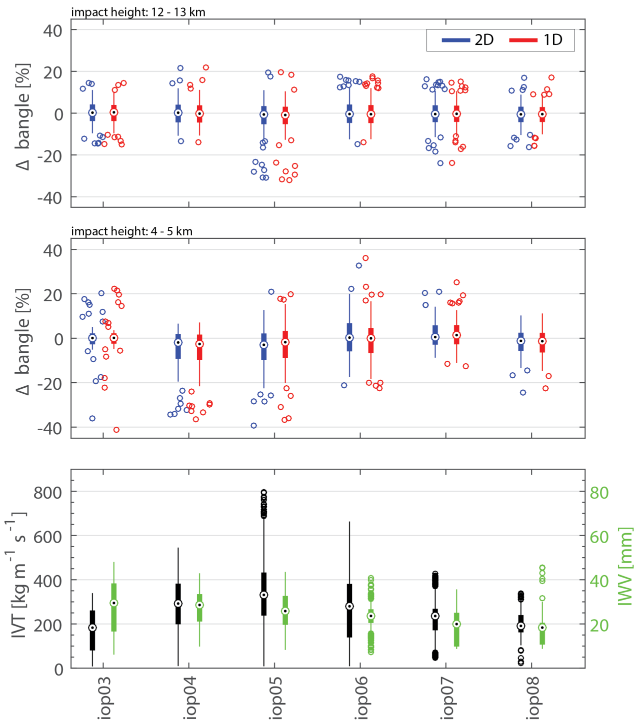

Figure 7. Boxplots showing observed minus simulated bending angle deviations for individual IOPs computed at two representative impact height levels: (top) within 12-13 km of the profile top, and (middle) between 4-5 km in the troposphere. (bottom) IVT magnitudes and corresponding IWV values are from ERA5. The thick line indicates the interquartile range, and the thin line shows minimum and maximum values excluding points falling outside 1.5 times the interquartile range, shown as circles.

statistics computed separately for individual IOPs at two impact height levels: (1) at 12-13 km, which is representative of the top of ARO profiles, and (2) at 4-5 km, representative of the lower troposphere. Statistics are supported by analyzing IWV values and IVT magnitudes which characterize the strength of AR conditions, where the value of IVT and IWV is extracted from the ERA5 at the location of the reference tangent point (lowermost profile point). The spread in bending angle deviations at 4-5 km, in terms of the interquartile range (thick line), is larger for IOP05 and IOP06 that are both relatively strong AR environments with the maximum IVT (thin line) reaching or exceeding 600 kg m^{-1} s^{-1} (Fig. 7). In contrast, the bending angle deviation for IOP07 and IOP08 are significantly smaller, which have both lower IVT and lower IWV. Bending angle measurements at 4-5 km impact height are likely more susceptible to loss of lock or multipath errors due to moisture gradients in the troposphere for the phased-locked loop GNSS receivers at the lowest part of the profile. Visual inspection of individual profiles based on Fig. 8 reveals larger deviations between observed and simulated bending angles than between 1D and 2D simulations, which are generally in close agreement. Some of the largest differences are shown for IOP04 and are associated with the height of the upper level temperature inversions at about 6-7 km altitude.

The ARO retrieval method utilizes in-situ measurements as a constraint in both the bending angle inversion and the refractivity inversion (Cao et al., 2024). Any error in the in-situ meteorological sensor on-board the aircraft, can affect the overall bending angle statistics due to the non-negligible contribution of errors in refractivity at the top

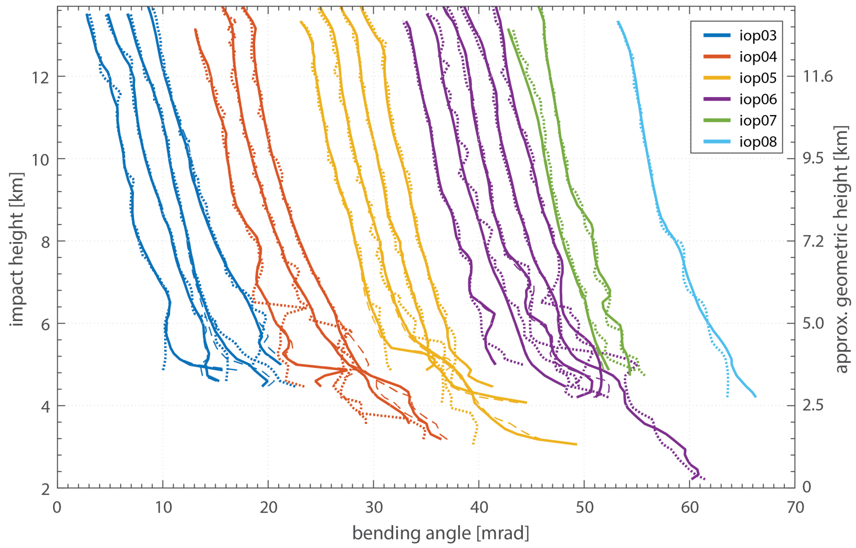

Figure 8. Profiles of observed bending angles (dotted line) for which the individual deviations at 4-5 km impact height relative to 2D simulations (solid line) exceed the corresponding one sigma standard deviation based on statistics for all occultations during six IOPs. Results for 1D simulations are presented for reference (dashed line). Consecutive profiles within each IOP are shifted by 2 mrad for visibility, while the first profiles for given IOPs are separated by 10 mrad.

of a given ARO profile to the retrieval. We investigate whether observations that have large differences relative to simulations are profiles that have unreliable in-situ measurements. Unreliable in-situ measurements (e.g. due to a malfunctioning humidity sensor) would show up as a large difference between in-situ and retrieved ARO refractivity at the top of the profile (green points in Figure 9). These might also be expected to show up as large differences between in-situ and ERA5 (orange points in Fig. 9). For the most part, high agreement between retrieved and measured refractivity values can be explained by the fact that the ARO retrieval method utilizes in-situ measurements as a constraint in both the bending angle inversion and the refractivity inversion. The median shows unbiased characteristics throughout all six IOPs with relatively small spread in terms of interquartile range. The refractivity statistics should be contrasted with bending angle deviations computed at the upper impact height level in Fig. 7 to determine whether uncertainties in in-situ values could account for large bending angle errors. Figure 7 shows a relatively large sample of outliers with underestimated observations of bending angle relative to forward modeled profiles, especially for IOP05. The in-situ refractivity differences show outliers of ± 2-3 % relative to retrieved as well as ERA5 values. However, they are not specific to IOP05 nor are they large enough to account for -25 % bending angle differences in Fig. 7 so we conclude that uncertainties in in-situ measurements are not responsible.

The fairly distinctive positive bias for IOP08 with overall larger spread in the refractivity should be regarded as a result of inaccurate representation of the atmospheric state since ARO retrieved values agree well with the observed in-situ values. The other IOPs all have outliers with relatively large differences, with no systematic explanation. The flights transition across the tropopause between Hawaii and the furthest northern points on the flight track, which in IOP04 to IOP07 reach the upper level trough. This could create highly variable temperature and/or tropopause height in the in-situ and ARO measurements that may not be reflected in the reanalysis fields.

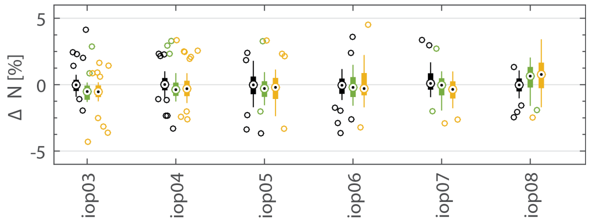

Figure 9. Refractivity deviations in percentage at the aircraft height for each IOP computed as (black) retrieved minus in-situ, (green) retrieved minus ERA5 and (orange) in-situ minus ERA5.

6 Analysis of forward modeling errors

The methods for simulating the bending angle used by the forward model (observation operator) are not exact and thus contribute to errors when analyzing the bending angle deviations. There are two main approximations to consider: (1) the approximation of spherical symmetry made in the 1D observation operator, and (2) the approximation of a vertical profile when the tangent points are drifting horizontally. We examine these approximations for a particularly challenging case where there is a strong vertical gradient in refractivity of limited horizontal extent. The occultation in question is on the northeast side of the IOP04 flight track in Fig. 1. The tangent point drifts towards the northwest, from the highest tangent point at the flight track to the lowest tangent point at 37.19°N, 170.57°W, across an elongated IVT feature with IWV ~25 mm and IVT > 375 kg m^{-1} s^{-1}. A slice of the refractivity field calculated from the ERA5 is used for the 2D ray-tracing for the lowest tangent point (Fig. 10). It clearly indicates an inversion layer in the lowermost troposphere manifested by a vertical gradient dN/dz = -130 km^{-1}. The lowest penetration depth of the observed ARO profile coincides with the top of the inversion layer at ~3 km impact height.

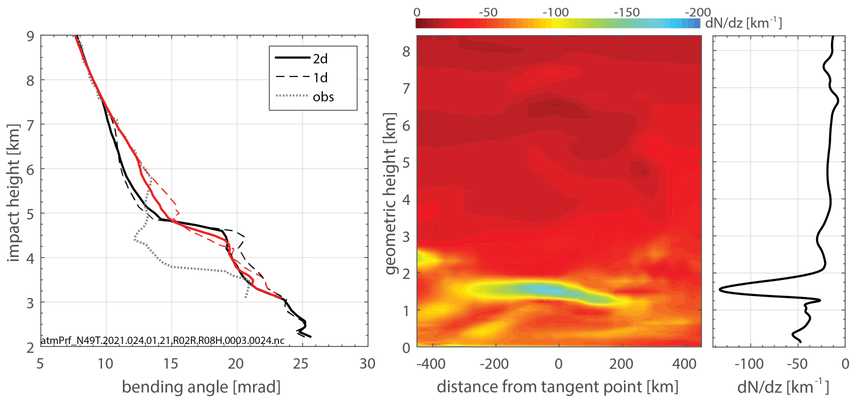

Figure 10. (left) Observed bending angle profile (dotted line) at 37.2°N, 170.5°W during IOP04 simulated with tangent point drift (red line) and without tangent point drift (black line). Simulations in a 2D atmosphere are marked with solid lines, while 1D results are shown in dashed lines. (middle) 2D field of vertical refractivity gradient (dN/dz) with respect to geometric height. The approximate correspondence to impact height is achieved by scaling the vertical extent of both figures. (right) The profile of dN/dz at the center of the refractivity field shown in the middle panel.

The atmospheric variability is reflected in the differences among simulated bending angles when incorporating tangent point drift (black) versus ignoring tangent point drift (red) in Fig. 10. In map view in Fig. 1 for IOP04 the tangent points at high altitudes near the aircraft location drift into a region of higher IVT and moisture at intermediate heights (see supplemental material). The higher moisture corresponds to higher refractivity which likely explains why the bending angle calculated with tangent point drift (red) is greater than the bending calculated without tangent point drift (black) in the impact height range from ∼7.5 km down to about 5 km. The observations closely match the bending angle profiles simulated with the tangent point drift above 6 km impact height. This demonstrates high sensitivity of ARO observations to atmospheric features in the middle troposphere that can be well captured even with a closed-loop GNSS receiver as previously demonstrated in the example in Fig. 5. The effect of tangent point drift contributes to 10 % bending angle differences at 6.5 km impact height even though the horizontal variations in refractivity gradient do not appear to be large at that height (Fig. 10 center).

The observed profile deviates significantly from all of the simulated profiles below 5 km impact height, where the simulations indicate a steep increase in bending angle. The change in gradient near that height could lead to multipath potentially causing cycle slips in the receiver tracking. This ultimately produces unreliable observations below 5 km height with less accumulated delay and less bending. This type of error could likely be eliminated in the future with open loop processing of the GNSS signal recorder data.

The effect of horizontal inhomogeneity in the refractivity field thus produces an error in simulated bending angle when the tangent point drifts across regions with varying atmospheric properties, and produces an error due to the integration along the ray-path where the ray-path traverses horizontally varying structure. This was anticipated based on simulations in an idealized cold frontal structure (Xie et al., 2008), and are seen here to occur in the more realistic ERA5 representations of the refractivity field in an AR. The two effects are studied separately to assess their individual contributions for the entire dataset based on specific configurations of the ARO forward model.

6.1 Effect of tangent point drift

In order to improve the computational efficiency of RO forward models, the impact of tangent point drift can be tested by assuming a single representative location for retrieved profile. For ARO, the reference tangent point position provided in the global attributes for the data products is the location of the lowest tangent point observed in the profile. Figure 11 shows the tangent point drift for ARO calculated as a difference between uppermost and lowermost observed points in each profile for the six IOPs of AR Recon 2021. The drift is on average ∼350 km and can occasionally reach 700 km, suggesting that its contribution should not be neglected when the atmosphere varies horizontally. The 2D operator requires refractivity information extracted from an atmospheric model in a 2D plane along to the ray-path and calculates the bending angle for all ray paths assuming the tangent point does not drift. We assess this assumption with two simulation experiments. The non-drifting tangent point experiment uses the reference tangent point position at the lowest point for all ray-paths. For the drifting tangent point experiment, for each tangent point in the profile, we extract a different 2D planar refractivity at the location of the individual tangent point, perform the simulation for bending angle using the 2D operator, extract the bending corresponding to the height for that individual ray-path, then move to the next tangent point location in the profile and repeat the procedure.

The assumption of no tangent point drift for ARO is more valid in the lower troposphere where tangent points are closer to the reference tangent point location. This

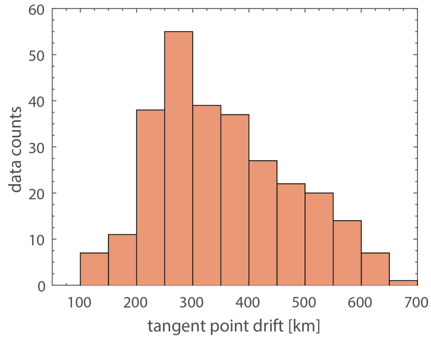

Figure 11. Histogram showing the tangent point drift calculated as a difference between uppermost and lowermost points for each ARO retrieval collected during the six IOPs of AR Recon 2021.

is reflected in the statistics presented in Fig. 12 as the impact of tangent point drift in the middle to the lower troposphere is shown to be relatively small generally, with relative bending angle standard deviation not exceeding 1.5 %. Since the tangent point drift in ARO retrievals generally increases with height and becomes the most significant at the upper levels, the disagreement in the simulated bending angles can exceed 5 % standard deviation and lead to -1.5 % bias at 13 km. The effect of tangent point drift at the top of the profile could be mitigated by choosing a reference tangent point that is more representative for the upper level retrievals, at the expense of introducing errors at lower tangent points. The assumption of no drift could reduce the computational cost of implementing the 2D forward model for ARO. However, the additional cost of the 2D drifting tangent point location for ARO is not prohibitive given that the total number of tangent points per profile is generally less than 150 given that heights are limited to ∼14 km with the diffraction limited vertical resolution of ∼100 m for the geometrical optics retrieval.

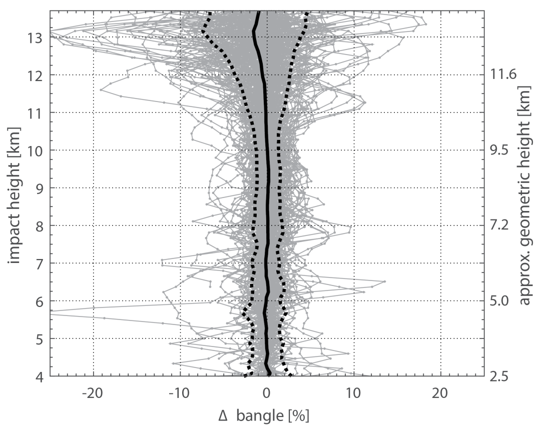

Figure 12. Bending angle differences in fractional units between 2D simulations without and with tangent point drift (drifting minus non-drifting). Grey lines correspond to bending angle differences for individual profiles, the solid black line is the mean difference and dotted black lines show standard deviation.

6.2 Effect of horizontal gradients

In order to assess the effect of horizontal refractivity gradients on bending angle profiles, results from two simulation schemes are compared based on forward modeling with the 2D operator. To distinguish the errors from those described in the previous section, the bending angles are simulated without considering the tangent point drift. The refractivity field used in the 2D simulation scheme is centered at the location of reference tangent point, and 15 profiles on either side are extracted in the occultation plane, as described in Section 4. In the corresponding 1D simulations, the central profile is replicated for 31 locations along the occultation plane replacing the horizontally varying refractivity field. The bending angles are simulated on a predefined impact height grid with exponentially varying vertical spacing of 120–190 m below 10 km. Figure 13 shows that contributions of horizontal gradients are generally small at the upper levels, resulting in 1 % standard deviation. Some profiles, however, have as much as 3-4 % deviation, likely associated with the tropopause. Below 10 km the deviations increase as the impact height decreases up to 5 % at 4 km impact height. The standard deviation between the 1D and 2D simulations computed within 4-5 km impact height is 3.75 %. This can be contrasted with corresponding bending angle deviations for ARO observations in Fig. 7, which have standard deviations of 8.34 % and 7.75 % relative to 1D and 2D simulations, respectively. The assessment of bending angle deviations due to horizontal refractivity inhomogeneities suggests that the application of the 2D forward model should be advantageous for assimilation of ARO observations. Below 4 km the deviations rapidly increase to exceed ±20 % in the lowermost 2 km. The variations are mostly driven by large bending angle magnitudes (Sokolovskiy, 2003) caused by sharp inversion layers that are recognized to produce negative biases in spaceborne RO retrievals of refractivity in the presence of super-refraction (Beyerle et al., 2006; Ao, 2007). In order to mitigate this effect, in the operational use at Naval Research Lab (NRL) and ECMWF, the ROPP operator terminates simulating the profile below super-refraction layers indicated by vertical refractivity gradient less than -157 km^{-1} (Ruston & Healy, 2021).

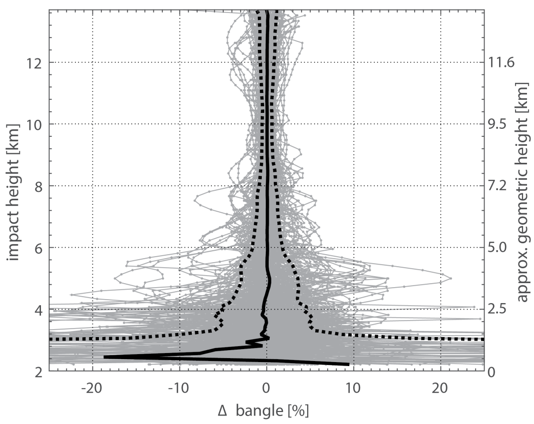

Figure 13. Bending angle differences in fractional units computed as 1D minus 2D simulations showing the effect of horizontal inhomogeneities. Grey lines correspond to bending angle differences for individual profiles for all eight IOPs, the solid black line is the mean difference and dotted black lines show standard deviation.

7 Analysis of bending angle profiles in atmospheric rivers

We hypothesized that the 2D bending angle operator would show large difference with respect to 1D in the vicinity of an AR because of the strong horizontal gradients of moisture associated with the AR water vapor transport, and temperature gradients across the cold front. While this is ambiguous in Fig. 7 when broken down by IOP during a sequence of flights in 2021, the previous section suggests the moisture component of IVT (i.e. IWV) predominantly affects the deviations. We find that there are strong effects for a specific case where the transect of ARO observations crossed perpendicular to the AR core. Figure 14 shows the deviations between 1D and 2D bending angles simulated with the effect of tangent point drift as a transect of profiles.

The transect crosses the drier region of high pressure south of the AR (A1), then crosses perpendicular to the AR tail (A2), then crosses back across the AR (A3), and then back across the high pressure (A4). The deviations are small for all profiles with low IVT, with the exception of occultation 026.00.20.G07, and are larger for transects A2 and A3 within the AR. In general, the occultations which cross the AR in transect A2 and A3 that are shown in red, for high IVT, have higher deviations than those in the surrounding regions. 45 % of the profiles within the AR have bending angle deviations greater than 5 % compared to 7 % of the profiles outside the AR. The largest deviations are between heights of 3–7 km (4–8 km impact height). Note that in the simulation, the observation operator is only run over the height range captured by observations.

Dropsondes were released during transects A2 and A3 of the flights. The dropsonde profile refractivity anomalies for transect A2 and A3 are shown in Figure 14b. Refractivity anomaly is the difference between the dropsonde refractivity and the refractivity climatology for the month of January from the CIRA-Q model (Kirchengast G & W, 1999). Below 9 km, the moisture term dominates in the refractivity anomaly (B. Murphy et al., 2015). The regions shaded in red in panel (b) are the moisture rich boundary layer and the low level jet rising up to 3 km height in the AR core, similar to the spatial characteristics found by Haase et al. (2021). In this case, a dry intrusion (Raveh-Rubin & Catto, 2019) can be seen behind the cold front on the north side of the AR, indicated in blue shading from 1-2 km in the center of the panel. In A3, the dropsonde in the deepest part of the AR core indicates moisture reaching up to 3 km. Interestingly, the ARO profile nearest that dropsonde (025.22.46.G24) extends to the surface. The tendency for RO profiles in the AR core to penetrate deeper was observed in previous studies (Murphy Jr & Haase, 2022), probably because vertical mixing smooths out sharp vertical gradients that would otherwise cause multipath propagation and signal tracking loss.

The mid-to-upper level features of the vertical structure in the dropsonde profiles tend to increase with height moving away from the center of the diagram, as indicated by the blue shading and slanted blue lines. The center point of the diagram corresponds to the furthest north point where the aircraft completed transect A2 and started A3. For example, sharp gradients associated with dry layers can be tracked from one profile to the next. The height of the low level moisture in the AR changes with distance along the transect as well. Similarly the height of the maximum deviation between 1D and 2D varies from one profile to the next, as well as the height of the lowest tangent point.

Profile 026.00.20.G07 has a sharp positive deviation at 3.1 km altitude. Transects A1 and A4 cross the high pressure outside the AR so there is not a lot of moisture to cause large horizontal variations. These transects are far from the temperature variations across the cold front, so these transects are in areas where the 1D and 2D simulations give close results. Occultation 026.00.20.G07 is a long occultation whose lowest ray-paths sample back towards the AR, so that sharp positive deviation could be indicating that it samples a dry layer at a different height.

This example shows that for a case (IOP06) where the flow within the AR is simple and the sampling geometry is advantageous, it is possible to make a direct link between the horizontal variations of refractivity and the deviations between 1D and 2D bending angle simulations. For these cases, it is expected that implementing the newly developed 2D bending operator will produce superior results in data assimilation experiments. In this sequence of flights, only IOP06 flew across the core of a well-formed AR. The other flights (IOP03-IOP05) are sampling regions of tropical moisture export, which can also have high IWV and IVT but are more difficult to interpret. Two of the flights (IOP07-IOP08) sampled primarily in the 500 hPa trough associated with the low pressure system with less moisture overall.

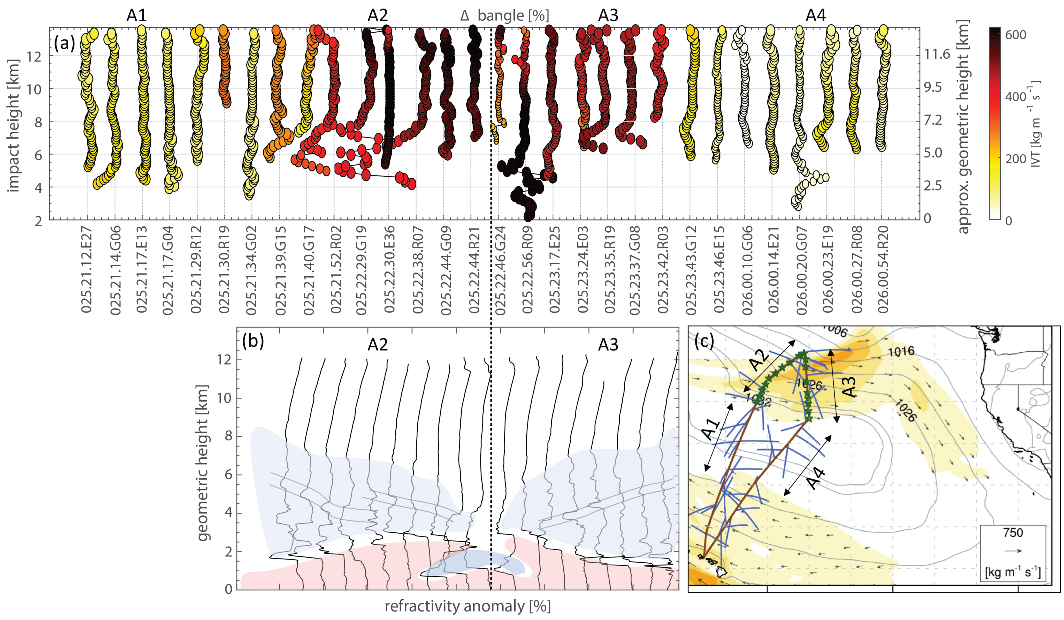

Figure 14. (a) Deviations between 1D and 2D bending angles simulated with tangent point drift for occultations along the transects across the AR indicated by A1, A2, A3, A4 as shown in panel (c). Each profile is shifted by 10 %. Individual tangent points are color-coded by the IVT beneath that point, and the size of each dot is scaled to corresponding IWV values. (b) Refractivity anomalies (observation minus climatology) for the dropsondes in transects A2 and A3. (c) Location of occultation profiles along transects A1 (outside the AR), A1 and A2 (inside the AR) and A4 (outside the AR).

8 Conclusions

The modification of the 2D forward model for ARO bending angle observations opens up a wide range of new applications for improved weather prediction using airborne and balloon-borne platforms. Because of the strong gradients in temperature and humidity found in ARs and their associated cold fronts, a sophisticated approach utilizing a two-dimensional structure of the atmosphere has been adopted in the forward model. The forward model is used to assess the importance of both vertical and horizontal refractivity inhomogeneities to simulating ARO bending angle observations. Since the tangent point drift in ARO profiles is on average 350 km and can occasionally exceed 700 km, the profile cannot be assumed to be vertical. The contribution of tangent point drift in a horizontally varying structure to forward modeling errors has been addressed by considering the values of bending angle at observed impact heights as individual observations rather than a single vertical profile in the forward simulations. Neglecting this effect is shown to contribute to bending angle deviations that exceed 5 % in terms of standard deviation. Previous work used the approach of assimilating 2D varying excess phase (X. M. Chen et al., 2018) or refractivity (Haase et al., 2021), which were both based on retrieving partial bending angle, defined as the portion of the bending accumulated below the aircraft flight altitude (Haase et al., 2014). This work demonstrates that there is significant reduction in error at the top of the profile if the full bending angle is used rather than partial bending. The application of a 2D operator is advantageous in simulating ARO profiles in the lower troposphere where the bending angle deviations can exceed 20 % relative to the simulations assuming a spherically symmetrical atmosphere. This will benefit future AR Recon campaigns once the open-loop tracking capability is available for ARO observations. With the current penetration depth of ARO profiles, typically down to 4 km impact height, the disagreement between 2D and 1D bending angles can reach 5 % in terms of standard deviation. The analysis of specific ARO profiles crossing an AR region characterized by high IVT magnitudes suggests that improvements on the order of 10 % are also expected in the middle troposphere due to the application of the 2D operator. While the use of the 2D forward model contributes to the overall complexity of the algorithm and reduces its computational efficiency, to date the increased cost has not been shown to be prohibitive for RO applications in NWP.

Data and software availability

The ARO data is available at `https://agsweb.ucsd.edu/gnss-aro/`. The dropsonde data is available at `https://cw3e.ucsd.edu/arrecon_data/`. The ROPP 2D operator is maintained and licensed by the EUMETSAT Radio Occultation Meteorology Satellite Application Facility (ROMSAF) at `https://rom-saf.eumetsat.int/ropp/`. The airborne radio occultation observation operator which relies on access to a ROPP license is available on request at `https://github.com/jhaaseresearch/sio-ropp`.

Acknowledgments

This work was carried out at the Scripps Institution of Oceanography, University of California San Diego, as part of the Atmospheric Rivers Program funded by the California Department of Water Resources. Paweł Hordyniec was supported in part by the Polish National Agency for Academic Exchange as part of the Bekker programme under the project entitled "Remote sensing of the atmosphere with airborne GNSS radio occultations" (PPN/BEK/2020/1/00250/U/00001). ARO data collection was made possible through Atmospheric Rivers Reconnaissance, a research and operations partnership between the Center for Western Weather and Water Extremes (CW3E) and the National Center for Environmental Prediction (NCEP). The primary facilities partners that make AR Recon possible are the United States Air Force Reserve Command 53rd Weather Reconnaissance Squadron and the NOAA Aircraft Operations Center. We thank the NOAA AOC for making observations possible from the NOAA G-IV and assisting in operation of the receivers. We thank the forecast and flight design teams and flight crews in planning and executing the targeted observation missions for the data collected for this paper, and Natalie Contreras (SIO) for assistance with data management. Additional funding for data collection and development of the ARO observation capability at Scripps was provided by NSF GRANT AGS-1642650 and AGS-1454125, NASA GRANT NNX15AU19G, and through a CW3E collaboration from the US Army Corps of Engineers. We would like to thank Sean Healy (ECMWF, UK) for his suggestions regarding potential modification of the existing 2D forward model for spaceborne RO. Dropsonde data were funded by AR Recon and made available by the NOAA Office of Marine and Aviation Operations (OMAO), and ERA5 reanalysis data were provided by the ECMWF. Additional computational resources were provided by the CW3E COMET computer facility and the NSF Cheyenne HPCMP facilities.

References

Adhikari, L., Xie, F., & Haase, J. S. (2016). Application of the full spectrum inversion algorithm to simulated airborne gps radio occultation signals. *Atmo-*

spheric Measurement Techniques, *9*(10), 5077–5087. doi: 10.5194/amt-9-5077-2016

Anthes, R., & Schreiner, W. (2019). Six new satellites watch the atmosphere over Earth's equator. *EOS*, *100*. doi: 10.1029/2019EO131779

Ao, C. (2007). Effect of ducting on radio occultation measurements: An assessment based on high-resolution radiosonde soundings. *Radio Science*, *42*(2). doi: 10.1029/2006RS003485

Aparicio, J. M., Deblonde, G., Garand, L., & Laroche, S. (2009). Signature of the atmospheric compressibility factor in cosmic, champ, and grace radio occultation data. *Journal of Geophysical Research: Atmospheres*, *114*(D16). doi: 10.1029/2008JD011156

Basha, G., & Ratnam, M. V. (2009). Identification of atmospheric boundary layer height over a tropical station using high-resolution radiosonde refractivity profiles: Comparison with gps radio occultation measurements. *Journal of Geophysical Research: Atmospheres (1984–2012)*, *114*(D16). doi: 10.1029/2008JD011692

Beyerle, G., Gorbunov, M., & Ao, C. (2003). Simulation studies of gps radio occultation measurements. *Radio Science*, *38*(5). doi: 10.1029/2002RS002800

Beyerle, G., Schmidt, T., Wickert, J., Heise, S., Rothacher, M., König-Langlo, G., & Lauritsen, K. (2006). Observations and simulations of receiver-induced refractivity biases in gps radio occultation. *Journal of Geophysical Research: Atmospheres*, *111*(D12). doi: 10.1029/2005JD006673

Cao, B., Haase, J. S., Murphy, M. J., Alexander, M. J., Bramberger, M., & Hertzog, A. (2022). Equatorial waves resolved by balloon-borne global navigation satellite system radio occultation in the strateole-2 campaign. *Atmospheric Chemistry and Physics*, *22*(23), 15379–15402. doi: 10.5194/acp-22-15379-2022

Cao, B., Haase, J. S., Murphy, M. J., & Willson, A. M. (2024). An airborne radio occultation dataset retrieved from multi-global navigation satellite systems in atmospheric river reconnaissance campaigns over the northeast pacifi (to be submitted). *Atmospheric Measurement Technique*.

Chen, S., Reynolds, C. A., Schmidt, J. M., Papin, P. P., Janiga, M. A., Bankert, R., & Huang, A. (2022). The effect of a kona low on the eastern pacific valentine's day (2019) atmospheric river. *Monthly Weather Review*, *150*(4), 863–882. doi: 10.1175/MWR-D-21-0182.1

Chen, X. M., Chen, S.-H., Haase, J. S., Murphy, B. J., Wang, K.-N., Garrison, J. L., . . . Xie, F. (2018). The impact of airborne radio occultation observations on the simulation of hurricane karl (2010). *Monthly Weather Review*, *146*(1), 329–350. doi: 10.1175/MWR-D-17-0001.1

Cucurull, L., Derber, J., & Purser, R. (2013). A bending angle forward operator for global positioning system radio occultation measurements. *Journal of Geophysical Research: Atmospheres*, *118*(1), 14–28. doi: 10.1029/2012JD017782

Cucurull, L., Derber, J., Treadon, R., & Purser, R. (2007). Assimilation of global positioning system radio occultation observations into ncep's global data assimilation system. *Monthly weather review*, *135*(9), 3174–3193. doi: 10.1175/MWR3461.1

Culverwell, I., Lewis, H., Offiler, D., Marquardt, C., & Burrows, C. (2015). The radio occultation processing package, ropp. *Atmospheric Measurement Techniques*, *8*(4), 1887–1899. doi: 10.5194/amt-8-1887-2015

Daingerfield, L. H. (1921). Kona storms. *Monthly Weather Review*, *49*(6), 327–329. doi: 10.1175/1520-0493(1921)49⟨327:KS⟩2.0.CO;2

Dettinger, M. D., Ralph, F. M., Das, T., Neiman, P. J., & Cayan, D. R. (2011). Atmospheric rivers, floods and the water resources of california. *Water*, *3*(2), 445–478. doi: 10.3390/w3020445

Eyre, J. (1994). Assimilation of radio occultation measurements into a numerical weather prediction system. *ECMWF, Tech. Memorandum*.

Eyre, J., Bell, W., Cotton, J., English, S., Forsythe, M., Healy, S., & Pavelin, E. (2022). Assimilation of satellite data in numerical weather prediction. part ii: Recent years. *Quarterly Journal of the Royal Meteorological Society*, *148*(743), 521–556. doi: 10.1002/qj.4228

Fjeldbo, G., Kliore, A. J., & Eshleman, V. R. (1971). The neutral atmosphere of venus as studied with the mariner v radio occultation experiments. *The Astronomical Journal*, *76*, 123. doi: 10.1086/111096

Geng, J., Chen, X., Pan, Y., Mao, S., Li, C., Zhou, J., & Zhang, K. (2019). Pride ppp-ar: an open-source software for gps ppp ambiguity resolution. *GPS solutions*, *23*, 1–10. doi: 10.1007/s10291-019-0888-1

Gershunov, A., Shulgina, T., Ralph, F. M., Lavers, D. A., & Rutz, J. J. (2017). Assessing the climate-scale variability of atmospheric rivers affecting western north america. *Geophysical Research Letters*, *44*(15), 7900–7908. doi: 10.1002/2017GL074175

Guan, B., Waliser, D. E., & Ralph, F. M. (2021). Global application of the atmospheric river scale. *Journal of Geophysical Research: Atmospheres*, e2022JD037180. doi: 10.1029/2022JD037180

Guo, P., Kuo, Y.-H., Sokolovskiy, S., & Lenschow, D. (2011). Estimating atmospheric boundary layer depth using cosmic radio occultation data. *Journal of the Atmospheric Sciences*, *68*(8), 1703–1713. doi: 10.1175/2011JAS3612.1

Haase, J., Murphy, B., Muradyan, P., Nievinski, F., Larson, K., Garrison, J., & Wang, K.-N. (2014). First results from an airborne gps radio occultation system for atmospheric profiling. *Geophysical Research Letters*, *41*(5), 1759–1765. doi: 10.1002/2013GL058681

Haase, J., Murphy, M., Cao, B., Ralph, F., Zheng, M., & Delle Monache, L. (2021). Multi-gnss airborne radio occultation observations as a complement to dropsondes in atmospheric river reconnaissance. *Journal of Geophysical Research: Atmospheres*, *126*(21), e2021JD034865. doi: 10.1029/2021JD034865

Healy, S. (2001). Radio occultation bending angle and impact parameter errors caused by horizontal refractive index gradients in the troposphere: A simulation study. *Journal of Geophysical Research: Atmospheres*, *106*(D11), 11875–11889. doi: 10.1029/2001JD900050

Healy, S., Eyre, J., Hamrud, M., & Thépaut, J.-N. (2007). Assimilating gps radio occultation measurements with two-dimensional bending angle observation operators. *Quarterly Journal of the Royal Meteorological Society*, *133*(626), 1213–1227. doi: 10.1002/qj.63

Healy, S., Haase, J., & Lesne, O. (2002). Letter to the editor abel transform inversion of radio occultation measurements made with a receiver inside the earth's atmosphere. In *Annales geophysicae* (Vol. 20, pp. 1253–1256). doi: 10.5194/angeo-20-1253-2002

Healy, S., & Thépaut, J.-N. (2006). Assimilation experiments with champ gps radio occultation measurements. *Quarterly Journal of the Royal Meteorological Society*, *132*(615), 605–623. doi: 10.1256/qj.04.182

Hersbach, H., Bell, B., Berrisford, P., Hirahara, S., Horányi, A., Muñoz-Sabater, J., ... others (2020). The era5 global reanalysis. *Quarterly Journal of the Royal Meteorological Society*, *146*(730), 1999–2049. doi: 10.1002/qj.3803

Kirchengast G, H. J., & W, P. (1999). The cira86aq_uog model: An extension of the cira-86 monthly tables including humidity tables and a fortran95 global moist air climatology model. *IMG/UoG Technical Report for ESA/ESTEC*, *8/1999*, 18.

Kursinski, E., Hajj, G., Schofield, J., Linfield, R., & Hardy, K. R. (1997). Observing earth's atmosphere with radio occultation measurements using the global positioning system. *Journal of Geophysical Research: Atmospheres (1984–2012)*, *102*(D19), 23429–23465. doi: 10.1029/97JD01569

Melbourne, W., Davis, E., Duncan, C., Hajj, G., Hardy, K., Kursinski, E., ...

Yunck, T. (1994). *The application of spaceborne gps to atmospheric limb sounding and global change monitoring* (Tech. Rep.).

Morrison, I., & Businger, S. (2001). Synoptic structure and evolution of a kona low. *Weather and forecasting*, *16*(1), 81–98. doi: 10.1175/1520-0434(2001)016⟨0081:SSAEOA⟩2.0.CO;2

Muradyan, P., Haase, J. S., Xie, F., Garrison, J. L., & Voo, J. (2011). Gps/ins navigation precision and its effect on airborne radio occultation retrieval accuracy. *GPS solutions*, *15*(3), 207–218. doi: 10.1007/s10291-010-0183-7

Murphy, B., Haase, J., Muradyan, P., Garrison, J., & Wang, K.-N. (2015). Airborne gps radio occultation refractivity profiles observed in tropical storm environments. *Journal of Geophysical Research: Atmospheres*, *120*(5), 1690–1709. doi: 10.1002/2014JD022931

Murphy, B. J. (2015). *Profiling the Moisture Environment of Developing Tropical Storms using Airborne Radio Occultation* (Doctoral Dissertation). Purdue University.

Murphy, M. J., Haase, J. S., Grudzien, C., & Delle Monache, L. (2024). The utility of a two-dimensional forward model for bending angle observations in regions with strong horizontal gradients (under review). *Monthly Weather Review*.

Murphy Jr, M. J., & Haase, J. S. (2022). Evaluation of gnss radio occultation profiles in the vicinity of atmospheric rivers. *Atmosphere*, *13*(9), 1495. doi: 10.3390/atmos13091495

Office, I. M. C. (2022). *The 2022 national winter season operations plan.* Retrieved from https://www.icams-portal.gov/resources/ofcm/nwsop/2022_nwsop.pdf

Poli, P. (2004). Effects of horizontal gradients on gps radio occultation observation operators. ii: A fast atmospheric refractivity gradient operator (fargo). *Quarterly Journal of the Royal Meteorological Society*, *130*(603), 2807–2825. doi: 10.1256/qj.03.229

Ralph, F. M., Cannon, F., Tallapragada, V., Davis, C. A., Doyle, J. D., Pappenberger, F., ... others (2020). West coast forecast challenges and development of atmospheric river reconnaissance. *Bulletin of the American Meteorological Society*, *101*(8), E1357–E1377. doi: 10.1175/BAMS-D-19-0183.1

Ralph, F. M., Iacobellis, S., Neiman, P., Cordeira, J., Spackman, J., Waliser, D., ... Fairall, C. (2017). Dropsonde observations of total integrated water vapor transport within north pacific atmospheric rivers. *Journal of Hydrometeorology*, *18*(9), 2577–2596. doi: 10.1175/JHM-D-17-0036.1

Ralph, F. M., Neiman, P. J., Wick, G. A., Gutman, S. I., Dettinger, M. D., Cayan, D. R., & White, A. B. (2006). Flooding on california's russian river: Role of atmospheric rivers. *Geophysical Research Letters*, *33*(13). doi: 10.1029/2006GL026689

Ralph, F. M., Rutz, J. J., Cordeira, J. M., Dettinger, M., Anderson, M., Reynolds, D., ... Smallcomb, C. (2019). A scale to characterize the strength and impacts of atmospheric rivers. *Bulletin of the American Meteorological Society*, *100*(2), 269–289. doi: 10.1175/BAMS-D-18-0023.1

Ramage, C. S. (1962). The subtropical cyclone. *Journal of Geophysical Research*, *67*(4), 1401–1411. doi: 10.1029/JZ067i004p01401

Raveh-Rubin, S., & Catto, J. L. (2019). Climatology and dynamics of the link between dry intrusions and cold fronts during winter, part ii: Front-centred perspective. *Climate Dynamics*, *53*(3-4), 1893–1909. doi: 10.1007/s00382-019-04793-2

Reynolds, C. A., Doyle, J. D., Ralph, F. M., & Demirdjian, R. (2019). Adjoint sensitivity of north pacific atmospheric river forecasts. *Monthly Weather Review*, *147*(6), 1871–1897. doi: 10.1175/MWR-D-18-0347.1

Rodgers, C. D. (2000). *Inverse methods for atmospheric sounding: theory and practice* (Vol. 2). World scientific.

ROM SAF, E. (2021). The radio occultation processing package (ropp) forward model module user guide. *SAF/ROM/METO/UG/ROPP/006*.

Ruston, B., & Healy, S. (2021). Forecast impact of formosat-7/cosmic-2 gnss radio occultation measurements. *Atmospheric Science Letters*, *22*(3), e1019. doi: 10.1002/asl.1019

Schreiner, W. S., Weiss, J., Anthes, R. A., Braun, J., Chu, V., Fong, J., … others (2020). Cosmic-2 radio occultation constellation: First results. *Geophysical Research Letters*, *47*(4), e2019GL086841. doi: doi.org/10.1029/2019GL086841

Simpson, R. H. (1952). Evolution of the kona storm a subtropical cyclone. *Journal of Atmospheric Sciences*, *9*(1), 24–35. doi: 10.1175/1520-0469(1952)009⟨0024:EOTKSA⟩2.0.CO;2

Smith, E. K., & Weintraub, S. (1953). The constants in the equation for atmospheric refractive index at radio frequencies. *Proceedings of Proc. IRE 41*, 1035–1037. doi: 10.1109/JRPROC.1953.274297

Sokolovskiy, S. (2003). Effect of superrefraction on inversions of radio occultation signals in the lower troposphere. *Radio Science*, *38*(3), 24–1. doi: 10.1029/2002RS002728

Tarek, M., Brissette, F. P., & Arsenault, R. (2020). Evaluation of the era5 reanalysis as a potential reference dataset for hydrological modelling over north america. *Hydrology and Earth System Sciences*, *24*(5), 2527–2544. doi: 10.5194/hess-24-2527-2020

Trémolet, Y., & Auligné, T. (2020). The Joint Effort for Data Assimilation Integration (JEDI). *JCSDA Quarterly*(66), 1–5. doi: 10.25923/RB19-0Q26

von Engeln, A., Healy, S., Marquardt, C., Andres, Y., & Sancho, F. (2009). Validation of operational GRAS radio occultation data. *Geophysical research letters*, *36*(17).

Wang, K.-N., Garrison, J., Haase, J., & Murphy, B. (2017). Improvements to gps airborne radio occultation in the lower troposphere through implementation of the phase matching method. *Journal of Geophysical Research: Atmospheres*, *122*(19), 10–266. doi: 10.1002/2017JD026568

Wang, K.-N., Garrison, J. L., Acikoz, U., Haase, J. S., Murphy, B. J., Muradyan, P., & Lulich, T. (2016). Open-loop tracking of rising and setting gps radio-occultation signals from an airborne platform: Signal model and error analysis. *IEEE Transactions on Geoscience and Remote Sensing*, *54*(7), 3967–3984. doi: 10.1109/TGRS.2016.2532346

Xie, F., Adhikari, L., Haase, J. S., Murphy, B., Wang, K.-N., & Garrison, J. L. (2018). Sensitivity of airborne radio occultation to tropospheric properties over ocean and land. *Atmospheric Measurement Techniques*, *11*(2), 763–780. doi: 10.5194/amt-11-763-2018

Xie, F., Haase, J. S., & Syndergaard, S. (2008). Profiling the atmosphere using the airborne gps radio occultation technique: A sensitivity study. *IEEE transactions on geoscience and remote sensing*, *46*(11), 3424–3435. doi: 10.1109/TGRS.2008.2004713

Xie, F., Wu, D., Ao, C., Mannucci, A., & Kursinski, E. (2012). Advances and limitations of atmospheric boundary layer observations with gps occultation over southeast pacific ocean. *Atmospheric Chemistry and Physics*, *12*(2), 903–918. doi: 10.5194/acp-12-903-2012

Zheng, M., Delle Monache, L., Cornuelle, B. D., Ralph, F. M., Tallapragada, V. S., Subramanian, A., … others (2021). Improved forecast skill through the assimilation of dropsonde observations from the atmospheric river reconnaissance program. *Journal of Geophysical Research: Atmospheres*, *126*(21), e2021JD034967. doi: 10.1029/2021JD034967

Zheng, M., Delle Monache, L., Wu, X., Ralph, F. M., Cornuelle, B., Tallapragada, V., … others (2021). Data gaps within atmospheric rivers over the northeastern pacific. *Bulletin of the American Meteorological Society*, *102*(3), E492–E524. doi: 10.1175/BAMS-D-19-0287.1